EVALUATION OF THE VELOCITY POTENTIAL-BASED FINITE-STATE MODEL FOR GROUND EFFECT USING A STATE-SPACE FREE VORTEX WAKE MODEL

Andro Metry
Graduate Research Assistant

J. V. R. Prasad
Professor

Georgia Institute of Technology
Atlanta, GA, USA

Cecilia Cannone
Visiting MS Student

Batin Bugday
Graduate Research Assistant

Umberto Saetti
Assistant Professor

University of Maryland
College Park, MD, USA

ABSTRACT

A velocity potential-based finite state model (VPBFSM) has been developed to analyze an isolated rotor in ground effect. The model uses mass source distributions to represent the ground and imposes the non-penetration of flow boundary condition. In this study, evaluations are performed by comparing the VPBFSM inflow distribution to that predicted by a high-fidelity free wake model for both full and inclined ground effect cases. The analysis is conducted for the UH–60 rotor using geometric and aerodynamic data from the literature. The VPBFSM exhibits good agreement with the free wake model in both ground effect cases, capturing the expected trend of decreasing inflow as the rotor approaches the ground, particularly on the side closest to the surface. Some discrepancies in magnitude are observed between the models; however, these remain acceptable, as they stem from the VPBFSM's reduced-order assumptions compared to the free wake model's higher geometric and wake fidelity.

NOTATION

a_n^{mc}, a_n^{ms}	Cosine and sine VPBFSM velocity potential states, respectively
h	Rotor height above ground normalized by R
H	Rotor height above ground, ft
i	Imaginary unit
m, r	Order of associated Legendre function, harmonic
n, j	Degree of associated Legendre function, radial
P_n^m, Q_n^m	Associated Legendre functions
$\bar{P}_n^m, \bar{Q}_n^m$	Normalized associated Legendre functions
R	Rotor radius, ft
r_0	Main rotor radial location
$[S]$	Pressure correlation matrix
t	Time, second
$[\hat{V}_m]$	Mass flow matrix
$\vec{v}$	Induced velocity vector, nondimensionalized by ΩR
$\vec{v}^{\dagger}$	Adjoint velocity vector, nondimensionalized by ΩR
Greek	
$\Delta_n^{mc}, \Delta_n^{ms}$	Cosine and sine costates, respectively
$\nu, \eta, \bar{\psi}$	Ellipsoidal coordinates
ξ	Streamline coordinate
ρ	Density of air $slug/ft^3$
τ_n^{mc}, τ_n^{ms}	Cosine and sine pressure coefficients, respectively
Φ_n^m	Pressure potential (shaping) function
Ω	Rotor rotating speed, rad/s
$\omega_n^{mc}, \omega_n^{ms}$	Cosine and sine pressure coefficients of ground rotor, respectively
δ	Inclination angle of the ground, degree
$(^*)$	Derivative with respect to nondimensional time, Ωt

INTRODUCTION

The demand for real-time helicopter flight simulation in ground effect has driven the development of reduced-order models that balance accuracy with computational efficiency. Among these, finite state wake models are widely used in rotorcraft inflow research due to their low computational cost and ease of implementation. However, their accuracy is limited in simulating maneuvering flights near the ground, particularly in cases involving inclined, partial, and dynamic ground effects.

When helicopters operate near ship decks, the ground, or building tops, they encounter various types of ground effect, including full, inclined, and partial. In full or normal ground effect, the rotor is entirely above a flat ground plane. Inclined ground effect refers to a case where the rotor is entirely above a sloped ground surface. Partial ground effect occurs when only part of the rotor disk overlaps with a ground surface, such as when hovering near the edge of a deck or building.

In these cases, ground proximity alters the flow field, typically increasing rotor thrust and reducing inflow for a given power consumption. To accurately capture these effects, the non-penetration of flow boundary condition — also known as the no-flux boundary condition — must be imposed at the ground or surface. This ensures that the modeled flow does not unrealistically pass through the boundary and allows for the correct prediction of inflow behavior.

Many studies have been conducted to understand and simulate the different types of ground effect. Within the finite state wake modeling framework, the most commonly used approaches for modeling ground effect include the image rotor method and pressure potential-based formulations (Refs. 1–5). The image rotor model automatically satisfies the non-penetration of flow boundary condition at the ground. This is achieved by mirroring the actual rotor below the ground to cancel the normal flow interaction at the ground plane. However, this method fails to accurately represent inclined ground, moving ground, or partial ground effects. A few studies (Refs. 3–5) in the past have modeled various cases of ground effect, including full, inclined, and partial, using a spatially distributed pressure perturbation over the footprint of the rotor, called the "ground rotor" at the ground plane. The ground's contribution is combined with the main rotor's pressure perturbation to calculate the rotor inflow in ground effect. These attempts showed good agreement with experimental data for steady ground effect cases. However, they could not model dynamic ground effect due to the limitations of state-of-the-art finite state inflow modeling at that time, which did not allow for explicit modeling of induced velocities off the rotor disk within the wake.

Using a velocity potential representation of the flow field, Morillo and Peters (Ref. 6), and Peters et al. (Ref. 7) developed the three-dimensional finite state model by applying the Galerkin approach, which allowed for computing flow velocities at any point within the rotor wake as well as above and on the rotor disk. Yu and Peters (Refs. 8–10) used the velocity potential-based finite state inflow modeling from Refs. (6, 7) along with the concept of a "ground rotor" pressure field from Refs. (3–5) to model various ground effect cases, including normal, partial, and dynamic. Additionally, Yu and Peters in Ref. (10) used a mass source distribution at the "ground rotor" with an exit pressure equal to that exerted by the rotor at the ground plane, which showed a good correlation with experimental data for various steady ground effect cases. However, they showed that quasi-steady modeling of dynamic ground effect would give rise to significant error. Unlike the image rotor approach, both ground effect finite state models in Refs. (5, 10) do not consider for the "non-penetration of flow boundary condition" at the ground in their formulations.

To address the limitation of existing finite state models (Refs. 5, 10), which do not enforce the non-penetration of flow boundary condition at the ground when studying isolated rotors in ground effect, Metry et al. (Ref.11) developed a velocity potential-based finite state model. This model represents the ground using mass source distributions in the flow field and explicitly enforces the non-penetration of flow boundary condition at the ground plane. In this approach, the ground rotor is modeled as a region significantly larger than the main rotor, and the mass sources are distributed at the ground rotor where the boundary condition is enforced within the main rotor wake radius.

The model in Ref. (11) makes use of the velocity potential-based finite state modeling for single rotors (Refs. 6, 7), ground effect modeling (Refs. 8–10), and coaxial rotors (Refs. 12, 13), where the lower rotor is treated as a non-lifting rotor with unknown mass source distribution strengths. Additionally, the size of the lower rotor is considered unknown and is determined from the ground boundary condition. Therefore, the model is formulated to compute the strength of the unknown mass source distributions and the size of the non-lifting ground rotor, using an optimization method to enforce the ground boundary condition.

However, the model developed in Ref. (11) is highly sensitive to several factors such as the initial guess of ground source distribution strengths for optimization, the number of mass source distributions, the number and location of collocation points at the ground plane, and the choice of ground rotor size.

To address these challenges, Metry, Prasad, and Peters in Ref. (14) developed an alternative approach for imposing the boundary condition at the ground without relying on optimization. They initially formulated a matrix relation to estimate the strengths of the ground mass source distributions in terms of the rotor loading. However, this relation failed to enforce the boundary condition effectively at the ground, as it excluded the $r = j$ terms (where r and j represent the Legendre function harmonic and radial terms, respectively) in the computation of the source strengths and ground flow velocities to avoid singularities (Refs. 6, 10). As a result, methods were developed within the model to adjust the estimated strengths of the mass source distributions and the ground rotor size to effectively impose the boundary condition and analyze the behavior of the R-50 unmanned helicopter rotor in normal, inclined, and partial ground effect cases. The results showed good agreement with expected physical trends for these ground effect cases. However, the need to adjust both source strengths and ground rotor size introduces sensitivity into the model's ability to satisfy the boundary condition and predict rotor inflow in ground effect. Therefore, a new approach is needed to impose the boundary condition more robustly.

Metry et al. in Ref. (15) incorporated the $r = j$ terms in the computation of the strengths of the mass source distributions and the ground rotor flow velocities. This eliminates the need for adjustments to the strengths or ground rotor size when enforcing the non-penetration of flow boundary condition at the ground. Additionally, the study shows good correlation for the average rotor inflow with the Hayden model (Ref. 16). However, the inflow distribution requires further validation against experimental data or a high-fidelity model to increase confidence in using the VPBFSM to predict the inflow distribution in ground effect.

In parallel with reduced-order models like the VPBFSM, free wake methods have been developed to capture rotor wake dynamics with higher fidelity. Emerging rotorcraft configurations, including those envisioned for Future Vertical Lift (FVL) and Urban Air Mobility (UAM), present complex aerodynamic interactions between multiple rotors and lifting surfaces. UAM vehicles, in particular, may operate at high and variable rotor speeds, which increases modeling fidelity requirements and computational cost. High rotor RPM demands finer time resolution; interaction modeling requires extended wake computations; and rigid rotors necessitate detailed structural dynamics. Although high-fidelity modeling is possible, achieving real-time or near-real-time performance for control development or simulation-based design remains challenging. Thus, it is critical to develop models amenable to linearization or reduction into first-order state-space form which is ideal for control applications and system analysis.

To this end, researchers have explored extracting linearized models from free-wake and vortex models using system identification (Refs. 17,18). A more direct method was introduced by Celi (Ref. 19), who formulated the University of Maryland Free Wake Model in first-order state-space form using the method of lines. This discretizes the wake evolution equations—originally PDEs—into ODEs by assigning a state to each wake node based on its age. The result is a time-evolving first-order ODE system, enabling linearization about a periodic equilibrium trajectory. Subsequent refinements incorporated vortex strength dynamics, wake dissipation through core growth, and a near-wake vortex lattice model (Refs. 20–22). The resulting state-space free-vortex wake model, coupled with a near-wake vortex lattice method, was validated by Bugday et al. (Ref. 23) against experimental measurements and high-fidelity simulations across key flight conditions, including hover, forward flight, and vortex ring state (VRS). In this study, the free wake model is extended to analyze an isolated rotor in ground effect using the image rotor method.

Ground effect in this study is modeled using the method of images, a widely adopted technique in rotorcraft simulations involving free-wake models (Refs. 24–26) extending to slope surfaces and partial ground effect (Ref. 5) as well as real time simulations (Ref. 27). This approach is favored for its simplicity, ease of implementation, and minimal computational overhead such that it does not require additional memory to store the image wake (Ref. 26) or introduce extra states in state-space formulations. In this method, one or more mirror images of the rotor wake (or portions thereof) are introduced into the Biot–Savart calculations. These mirrored wakes are arranged such that the vertical (normal) component of the induced velocity is canceled at the ground plane, ensuring that the wake does not artificially penetrate the ground boundary.

The focus of this paper is to correlate the inflow distribution predicted by the VPBFSM developed in (Ref. 15) with that of the free wake model. Additionally, this study aims to increase confidence in using the VPBFSM (Ref. 15) for analyzing rotor inflow in ground effect, particularly for full and inclined ground effect cases.

The paper is organized as follows: first, the formulation of the velocity potential-based finite state model (VPBFSM) for a dual-rotor system is presented, which is used to study an isolated rotor in full and inclined ground effect cases. Next, the methodology of the free wake model for analyzing an isolated rotor in full and inclined ground effect cases is described. Both models are then applied to the UH–60 helicopter rotor under steady-state conditions. Finally, the paper concludes with a summary of key findings and recommendations for future research.

VELOCITY POTENTIAL-BASED FINITE STATE MODEL

A detailed derivation for multi-rotor system using VPBFSM is presented in Refs. (12, 13). Thus, the derivation of this model is not attempted in this study. Instead, some review and modifications are included for the dual rotor velocity potential model to arrive at a single rotor and ground rotor. Also, the assumptions from Refs. (12,13) are retained in this model. They are as follows: the flow around the rotor disk is incompressible, inviscid, and uses a rigid cylindrical wake geometry.

Dual-Rotor VPBFSM Formulation

The governing equation of VPBFSM for the dual rotor is given in Eq. (1):

$$[M]^{+}\begin{Bmatrix}\{a_1{}^*\}\\\{\Delta_1{}^*\}\\\{a_2{}^*\}\end{Bmatrix}+[\hat{D}][\hat{V}_m][\hat{L}]^{-1}[\hat{M}]\begin{Bmatrix}\{a_1\}\\\{\Delta_1\}\\\{a_2\}\end{Bmatrix}=[\hat{D}]\begin{Bmatrix}\{\tau_1\}\\\{\tau_1^{\dagger}\}\\\{\tau_2\}\end{Bmatrix} \tag{1}$$

where:

$[\hat{M}]^{+} = \mathrm{diag}([\tilde{M}], -[\tilde{M}], [\tilde{M}])$,
$[\hat{M}] = \mathrm{diag}([\tilde{M}], [\tilde{M}], [\tilde{M}])$,
$[\hat{D}] = \mathrm{diag}([\tilde{D}], [\tilde{D}], [\tilde{D}])$,
$[\hat{V}_m] = \mathrm{diag}([\tilde{V}_m], [\tilde{V}_m], [\tilde{V}_m])$,
$[\hat{L}] = \mathrm{diag}([\tilde{L}(\tilde{X}_1)], [\tilde{L}(\tilde{X}_2)], [\tilde{L}(\tilde{X}_2)])$, and
$\tilde{X}_1 = \tan(\tilde{\chi}_1/2)$, $\tilde{X}_2 = \tan(\tilde{\chi}_2/2)$.

In Eq. (1), $\{a\}$ and $\{\Delta\}$ are vectors of velocity potential states and costates, respectively. Hence, in this formulation, the costate variable is introduced to compute the flow velocity below the rotor, while the state variable determines the flow velocity on and above the rotor disk. The adjoint equation of costates must be integrated backward in time as forward time-marching will make the system unstable due to the presence of a negative sign attached to the derivative term; the details of this method are mentioned in Ref. (12). Also, $\{\tau\}$ is a column vector consisting of pressure coefficients corresponding to load distribution or mass sources distributions; It is interesting to note that τ_n^m with $n+m = odd$ corresponds to pressure discontinuities while $n+m = even$ corresponds to mass sources terms (injection of flow into the flow field). $[\hat{M}]$, $[\hat{D}]$, $[\hat{V}_m]$, and $[\hat{L}]$ are apparent mass, damping, mass flow parameter and inflow influence coefficient matrices. These matrices are block diagonal and have analytical expressions similar to the single rotor velocity potential finite state model except $[\hat{V}_m]$ which is discussed in detail in Ref. (12). $\tilde{X}$ and $\tilde{\chi}$ are the wake skew function and the wake skew angle in radians, respectively, and can be computed using expressions in Ref. (12). It is important to note that $\{a^*\}$ and $\{\Delta^*\}$ are vectors of velocity potential state and costate derivatives with respect to nondimensional time, respectively. Furthermore, $\tau^\dagger$ is defined by $\tau^\dagger = (-1)^{j+1}\tau$, where j is the index of the radial distribution.

The pressure coefficients used in Eq. (1) can be computed using the following equations:

$$\tau_n^{0c} = \frac{1}{4\pi}\sum_{q=1}^{Q}\int_0^1 \frac{L_q}{\rho\Omega^2R^3}\Psi_n^0(\bar{r})d\bar{r} \tag{2a}$$

$$\tau_n^{mc} = \frac{1}{2\pi}\sum_{q=1}^{Q}\int_0^1 \frac{L_q}{\rho\Omega^2R^3}\Psi_n^m(\bar{r})d\bar{r}\cos(m\bar{\psi}_q) \tag{2b}$$

$$\tau_n^{ms} = \frac{1}{2\pi}\sum_{q=1}^{Q}\int_0^1 \frac{L_q}{\rho\Omega^2R^3}\Psi_n^m(\bar{r})d\bar{r}\sin(m\bar{\psi}_q) \tag{2c}$$

where L_q represents the sectional lift of qth blade in lbf/ft, Q is the number of blades, R is the rotor radius in ft, ρ is the freestream air density in $slug/ft^3$, Ω is the rotor rotational speed in rad/sec, $\bar{r}$ is the non-dimensional radial blade coordinate, ψ_q is the azimuthal angle of qth blade, and Ψ_n^m is the radial shaping function which has analytical formulation provided in Ref. (28). Note that uniform (τ_1^{0c}), fore-to-aft (τ_2^{1c}), and side-to-side (τ_2^{1s}) pressure coefficients are directly related to rotor thrust coefficient (C_T), aerodynamic pitch moment coefficient (C_M), and roll moment coefficient (C_L), respectively.

Modifications for Steady-State Ground Effect Analysis

Additional assumptions are made to the governing equation (Eq. 1) to study an isolated rotor in ground effect. First, the time-dependent terms $\{a^*\}$ and $\{\Delta^*\}$ in the governing equation are removed, as this paper focuses on the steady-state flow case. Second, the rotor is in hover so the $[L]^{-1}[\tilde{M}]$ results in identity matrix $[I]$. Finally, to distinguish between the pressure coefficient due to load distributions and mass source distributions, $\{\omega\}$ will be used instead of $\{\tau_2\}$ to represent the mass source distributions at the ground rotor. In other words, the main rotor and ground rotor (dual-rotor) are represented by load distributions $\{\tau_1\}$ and mass source distributions $\{\omega\}$, respectively. The velocity states of the ground will be represented as $\{c\}$ instead of $\{a_2\}$, r and j will represent harmonic and radial terms for the ground rotor instead of m and n, which represent the main rotor harmonic and radial terms, respectively.

Thus, Eq. (1) is modified and the final governing equation for steady state case is as follows:

$$[\hat{V}_m]\begin{Bmatrix}\{a_1\}\\ \{\Delta_1\}\\ \{c\}\end{Bmatrix} = \begin{Bmatrix}\{\tau_1\}\\ \{\tau_1^\dagger\}\\ \{\omega\}\end{Bmatrix} \tag{3}$$

where $\hat{V}_m$ is the mass flow parameter and can be simplified for axial and steady flow (Ref. 10) and defined here as follows:

$$\hat{V}_m = \begin{bmatrix} V & & & 0\\ & 2V & & \\ & & \ddots & \\ 0 & & & 2V\end{bmatrix}, \quad \text{where} \quad V = \sqrt{\frac{C_T}{2}} \tag{4}$$

After obtaining the states and co-states, two types of velocities are computed for each rotor. For instance, the main rotor will have a self-induced (self-flow) velocity and flow velocity of the main rotor at the ground. As discussed in Ref. (6), the on and above rotor-induced flow velocity is computed using a velocity potential relationship which is expanded in the ellipsoidal domain (see Appendix A) by employing the first and second kinds of the Legendre functions:

$$\vec{v} = \sum_{m=0}^{\infty}\sum_{n}^{\infty}(a_n^{mc}\Phi_n^{mc} + a_n^{ms}\Phi_n^{ms}) \tag{5}$$

where:

$$\Phi_n^{mc} = \bar{P}_n^m\bar{Q}_n^m\cos(m\bar{\Psi}) \tag{6a}$$

$$\Phi_n^{ms} = \bar{P}_n^m\bar{Q}_n^m\sin(m\bar{\Psi}) \tag{6b}$$

In the equations above, $\vec{v}$ is the induced flow velocity on or above a rotor, which can be used for the main rotor or the ground rotor. $\bar{P}_n^m$, and $\bar{Q}_n^m$ are the first and secondary normalized associated Legendre functions, respectively. The difference between the main rotor and the ground rotor in using Eq. (5) lies in identifying n in the second summation of this equation. For the main and ground rotors (Ref. 6), $n = m+1$ and $n = m+2$, respectively. As noted earlier, the main rotor's velocity states, radial, and harmonic terms are represented by a, m, and n, respectively, while for the ground rotor, they are represented by c, r, and j. For the ground rotor, $r = j+2$ is used instead of $n = m+2$, and terms where $r = j$ are initially excluded to avoid singularities (Refs. 6, 10).

Furthermore, to calculate the induced velocity below the rotor, an adjoint theorem has been developed and the detailed derivation of this theorem is discussed in Refs. (12, 29). For steady-state case, the adjoint theorem can be modified from the developed equation mentioned in Refs. (12, 29) by removing the time-dependent term. Figure 1 shows how to compute the induced velocity below the disk using the coordinate system displayed in this figure. For instance, induced velocity at point A $(\vec{v}_A)$ can be calculated using the velocity at point B

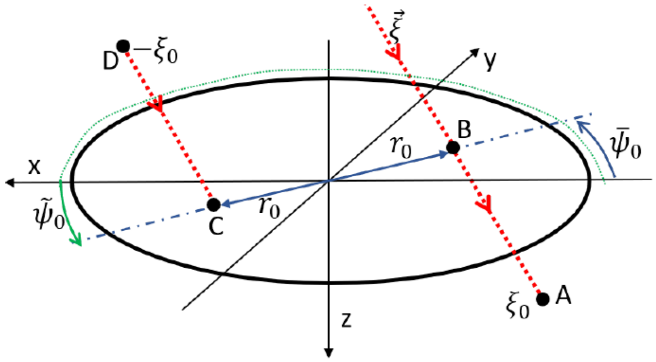

Figure 1: Coordinate system for computing induced velocity below the rotor, (Ref. 13).

($\vec{v}_B$), and the adjoint velocities at points C ($\vec{v}_C^{\dagger}$) and D ($\vec{v}_D^{\dagger}$), and can be defined as:

$$\vec{v}_A(r_0, \tilde{\psi}_0, \tilde{\xi}_0) = \vec{v}_B(r_0, \tilde{\psi}_0, 0) + \vec{v}_c^{\dagger}(r_0, \tilde{\psi}_0, 0) - \vec{v}_D^{\dagger}(r_0, \tilde{\psi}_0, -\tilde{\xi}_0) \tag{7}$$

It should be noted that since Eq. (7) ignores the time-dependent variable, there is no need for time marching backward to obtain the costate and then compute the ($\vec{v}_C^{\dagger}$) as mentioned in Ref. (12). This is because the costate will be equal to the state, and this means that $\vec{v}_C^{\dagger} = \vec{v}_B$. This is also one of the reasons that the system in Eq. (1) can be decoupled to arrive at Eq. (3).

Methodology for Ground Effect Modeling

After adapting the dual-rotor VPBFSM to study an isolated rotor in ground effect, the strengths of the mass source distributions must be determined to compute the velocity states and, consequently, the flow velocity of the rotors. These strengths are calculated to ensure the non-penetration of flow boundary condition is imposed at the ground. In this approach, the equation developed in Ref. (14) to estimate the strengths of the mass source distribution in terms of rotor loading is extended to include the $r = j$ terms. This is achieved by utilizing the approximate solution for the gradient of the velocity potential suggested in Ref. (30), as discussed in Appendix E. The complete equation is defined as follows:

$$\begin{gathered} \{\omega_j^r\} = [S_{jn}^{rm}]\,\{\tau_n^m\} \\ r = 0,\ 1,\ \ldots \quad j = r,\ r+2,\ r+4,\ \ldots \\ m = 0,\ 1,\ \ldots \quad n = m+1,\ m+3,\ \ldots \end{gathered} \tag{8}$$

where $[S_{jn}^{rm}]$ is the pressure correlation matrix relating the main rotor pressure loading to the strengths of the ground rotor mass source distributions through the orthogonality integrals of the associated Legendre functions. Since those integrals must be taken over a circular domain and are used to enforce the non-penetration of flow boundary condition, the ground is modeled as a rotor of a selected size. In this study, the ground rotor size is chosen to be the same as the main rotor size. For details on computing this correlation matrix and deriving Eq. (8), see Appendices C and D. Including the $r = j$ terms eliminates the need to adjust the mass source strengths and the ground rotor size, enabling effective enforcement of the boundary condition. However, this extension results in a higher ground effect on the main rotor, as shown in Ref. (15).

Several factors may contribute to the amplified ground effect prediction by the Velocity Potential Based Finite State Model. The model assumes incompressible, inviscid, irrotational flow and a cylindrical wake shape. In real flows, the wake undergoes contraction or expansion, while tip vortices diffuse as they move downstream. Upon reaching the ground, viscous diffusion causes part of the wake to expand more radially outward, while some of the flow recirculates due to interactions with the surface. However, the potential flow model lacks recirculation, viscosity, and turbulence, all of which dissipate energy in real-world conditions. Consequently, it overestimates the ground effect on the main rotor.

To address these challenges, an empirical correction factor is introduced in the velocity potential gradient, specifically for the $r = j$ terms. This factor reduces the influence of the sources on the main rotor, ensuring that the inflow distribution in ground effect is accurately captured. The correction factor was originally calibrated at a rotor height of $h = 1$, using the ground effect factor from the Hayden's model in the case study presented in Ref. (15), and is applied unchanged in the current study. Further details on its formulation and implementation are provided in Appendix E.

Full Ground Effect Case

Figure 2 illustrates the schematic setup used for modeling the hovering rotor in full ground effect, showing the arrangement of the rotor, ground plane, and computational elements. The strengths of the mass source distribution and the flow velocities are determined using the method detailed earlier in this section.

Inclined Ground Effect Case

Figure 3 shows the schematic for modeling a hovering rotor in inclined ground effect. In this study, a coordinate system is adopted to calculate the following velocities: the flow velocity of the main rotor on the ground, the self-flow (induced) velocity of the main rotor, the self-flow velocity of the ground rotor, and the flow velocity of the ground rotor on the main rotor.

The self-flow velocities of both the main rotor and ground rotor are computed using the same coordinate system as in the full ground effect case because each rotor operates within its frame of reference. To accurately account for the interaction between the main rotor and the inclined ground, the coordinate system is adjusted to account for the inclination of the ground along the z-axis. This adjustment ensures that the wake's z-axis remains vertical, even when the ground plane is inclined. The adjustment is expressed as

$$z = x\,\tan(\delta) + h \tag{9}$$

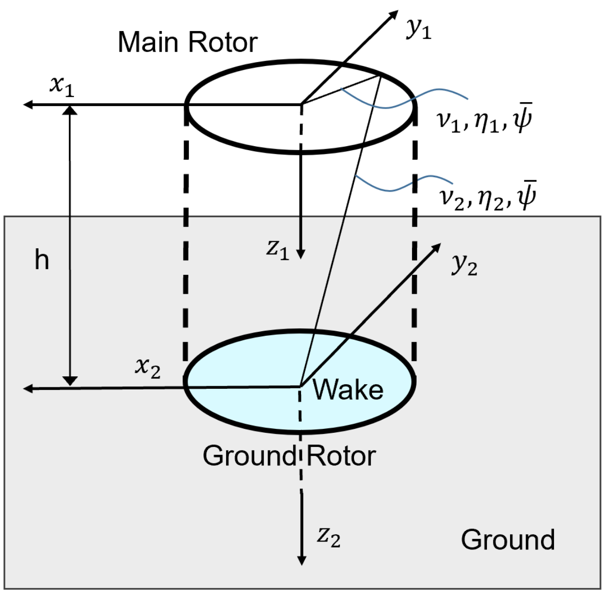

Figure 2: Schematic for modeling of hovering rotor in full ground effect.

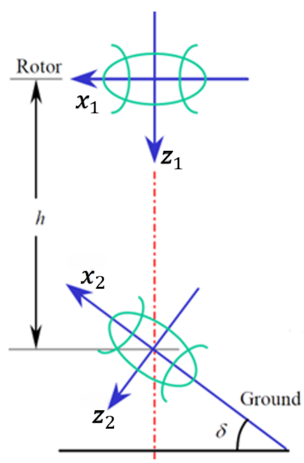

Figure 3: Schematic for modeling of hovering rotor in inclined ground effect.

where z is the $z-coordinate$ of point A (see Fig. 1), h denotes the non-dimensional rotor height above the ground, x represents the $x-axis$ coordinate of point A, and δ is the inclination angle of the ground.

Moreover, the total main rotor flow velocity is the sum of its self flow velocity and the velocity induced by the ground rotor. For an inclined ground plane, the non-penetration of flow boundary condition requires zero flow normal to the surface. As with the main rotor, the ground rotor's self flow velocity is purely normal. The main rotor induced velocity on the ground is inclined, so it is decomposed into a normal component and a tangential component. The normal component—obtained by multiplying the induced velocity by the cosine of the inclination angle—is added to the ground rotor self flow to obtain the total ground flow velocity and enforce zero normal flow. The tangential component produces edgewise flow, which does not affect the boundary condition and is therefore neglected in this study.

To compute the strengths of the mass source distributions correctly, the pressure correlation matrix is multiplied by the cosine of the inclination angle of the ground. Note that, in inclined ground effect, both zero and first harmonics for the mass source distributions are required to effectively impose the boundary condition at the ground, especially for high inclination angles. This is because the flow is no longer axisymmetric, unlike in the normal ground effect case.

FREE WAKE MODEL METHODOLOGY

Rotor Model

The rotor of the PSUHeloSim flight simulation code (Ref. 31) is used as a base for the implementation of the state-space free-vortex wake model. This rotor is representative of the rotor of a notional utility helicopter similar to the UH-60, and is based on Ref. (32). The model contains rigid flap and lead-lag rotor blade dynamics, a three-state Pitt-Peters inflow model (Ref. 33), and nonlinear aerodynamic lookup tables for the rotor blades. The rotor state vector is:

$$\boldsymbol{x}_{\mathrm{R}}^T = \big[\beta_0\ \beta_{1c}\ \beta_{1s}\ \beta_{0D}\ \dot{\beta}_0\ \dot{\beta}_{1c}\ \dot{\beta}_{1s}\ \dot{\beta}_{0D}\ \zeta_0\ \zeta_{1c}\ \zeta_{1s}\ \zeta_{0D}\ \dot{\zeta}_0\ \dot{\zeta}_{1c}\ \dot{\zeta}_{1s}\ \dot{\zeta}_{0D}\ \lambda_0\ \lambda_{1c}\ \lambda_{1s}\ \psi\big] \tag{10}$$

where:
$\beta_0,\ \beta_{1c},\ \beta_{1s},\ \beta_{0D}$ are the flapping angles in multi-blade coordinates,
$\zeta_0,\ \zeta_{1c},\ \zeta_{1s},\ \zeta_{0D}$ are the lead-lag angles in multi-blade coordinates,
$\lambda_0,\ \lambda_{1c},\ \lambda_{1s}$, are the main rotor induced inflow ratio harmonics, and
ψ is the azimuth angle of a reference blade. Note that when the rotor is two-way coupled with the free-vortex wake, the Pitt-Peters inflow states are bypassed and the induced velocities at each blade element as predicted by the free-vortex wake are used instead. The rotor control input vector is:

$$\boldsymbol{u}_{\mathrm{R}}^T = \big[\theta_{1c}\ \theta_{1s}\ \theta_0\ u\ v\ w\ p\ q\ r\ \dot{u}\ \dot{v}\ \dot{w}\ \dot{p}\ \dot{q}\ \dot{r}\ \Omega\ \dot{\Omega}\big] \tag{11}$$

where:
$\theta_{1c},\ \theta_{1s},\ \theta_0$ are lateral and longitudinal cyclic, and collective rotor inputs,
$u,\ v,\ w$ are the longitudinal, lateral, and vertical velocities in the body-fixed frame,
$p,\ q,\ r$ are the roll, pitch, and yaw rates in the body-fixed frame, and
Ω and $\dot{\Omega}$ are respectively the main rotor angular speed and acceleration.

State-Space Free-Vortex Wake Model with a Near-Wake Vortex Lattice Model

A state-space free-vortex wake model was implemented into the PSUHeloSim flight simulation code following the model of Refs. (34, 35). In PDE form, the trajectory of a wake node at non-dimensional time ψ and wake age ζ is governed by:

$$\frac{\partial \boldsymbol{r}(\psi,\zeta)}{\partial \psi} + \frac{\partial \boldsymbol{r}(\psi,\zeta)}{\partial \zeta} = \frac{1}{\Omega}\boldsymbol{V}\left(\boldsymbol{r}(\psi,\zeta)\right) \tag{12}$$

where the right-hand side is governed by the Biot-Savart law, which is the most expensive part of the free-wake computation. The wake model was implemented in the state-variable form generally following the approach of (Ref. 19), with some updates. Specifically, the model includes states to define vortex strength at each of the free wake nodes, allowing for varying vortex strength along the filament. A major update presented in this paper is the addition of a vortex-lattice model to represent near wake, including the shed vorticity and inboard vorticity distribution near the rotor blade. A vortex-lattice model with a large core size (0.05 R) is used to approximate vortex sheets trailing the rotor for a fraction of a revolution. The fundamental equations for the vortex lattice are similar to the tip vortex but use quadrilateral elements whose boundary condition is specified by the bound circulation on the blade elements of the rotor. The near wake model is implemented in state-variable form, similar to those presented in Ref. (23, 36). The near-wake extends only for a short distance behind the blade, after which it is assumed the vortex sheet rolls into a single-tip vortex which initiates at the end of the near-wake model. The resulting system of ODE expressed in dimensional time is:

$$\dot{\boldsymbol{r}}_{\text{NW}} = -\Omega \boldsymbol{A}_{\zeta}\boldsymbol{r}_{\text{NW}} + \boldsymbol{V}\left(\boldsymbol{r}_{\text{NW}}(t,\zeta)\right) \tag{13a}$$

$$\dot{\boldsymbol{r}}_{\text{TV}} = -\Omega \boldsymbol{A}_{\zeta}\boldsymbol{r}_{\text{TV}} + \boldsymbol{V}\left(\boldsymbol{r}_{\text{TV}}(t,\zeta)\right) \tag{13b}$$

$$\dot{\boldsymbol{\Gamma}}_{\text{NW}} = -\Omega \boldsymbol{A}_{\zeta}\boldsymbol{\Gamma}_{\text{NW}} \tag{13c}$$

$$\dot{\boldsymbol{\Gamma}}_{\text{TV}} = -\Omega \boldsymbol{A}_{\zeta}\boldsymbol{\Gamma}_{\text{TV}} \tag{13d}$$

where $\boldsymbol{r}_{\text{NW}}$, $\boldsymbol{\Gamma}_{\text{NW}}$, $\boldsymbol{r}_{\text{TV}}$, and $\boldsymbol{\Gamma}_{\text{TV}}$ represent the node positions and vortex strengths of the near wake and trailing vortex wake elements respectively. Matrix $\boldsymbol{A}_{\zeta}$ is the finite difference matrix corresponding to the 5PBU4 scheme from Ref. (19). The boundary conditions for the near wake elements are the locations and filtered bound circulation on the blade elements, and the boundary conditions for the trailing vortex elements are the position of the last outboard near wake element and the maximum vortex strength in the last row of near wake elements. As such, the coupled rotor and free-vortex wake dynamics are formulated as a system of ODEs where the state vector is constituted by the rotor states and the free-wake states such that:

$$\boldsymbol{x}^T = \begin{bmatrix}\boldsymbol{x}_{\text{R}}^T & \boldsymbol{x}_{\text{W}}^T\end{bmatrix} \tag{14}$$

where $\boldsymbol{x}_{\text{R}}^T$ is the rotor state vector and $\boldsymbol{x}_{\text{W}}^T$ is the rotor wake state vector:

$$\boldsymbol{x}_{\text{W}}^T = \begin{bmatrix}\boldsymbol{r}_{\text{NW}}^T & \boldsymbol{r}_{\text{TV}}^T & \boldsymbol{\Gamma}_{\text{NW}}^T & \boldsymbol{\Gamma}_{\text{TV}}^T & \boldsymbol{\Gamma}_{\text{b}}^T\end{bmatrix} \tag{15}$$

The control input vector is assumed to equal to the rotor control input vector such that $\boldsymbol{u} = \boldsymbol{u}_{\text{R}}$.

The wake model uses Scully's viscous core model, and the Lamb-Oseen core growth model to account for diffusion of the core due to viscous effects (Ref. 34). As shown in Ref. (34), the core size can be parameterized by the wake age as:

$$r_c = \sqrt{{r_0}^2 + \frac{4\alpha\delta\nu\zeta}{\Omega}} \tag{16}$$

In the state space implementation, each wake node is fixed at a particular age, and thus the core size can be pre-computed and remains constant for a given node throughout the simulations.

The coupled rotor and state-space free-vortex wake model is implemented in MATLAB®/Simulink. As illustrated in the flowchart presented in Fig. 4, the model is initialized with a prescribed wake representing an anticipated solution. The dynamics are integrated using the fifth-order Runge-Kutta (RK5) time integration method until they reach a periodic equilibrium. The wake states consist of vortex nodes and strengths associated with trailed tip vortices and near-wake vortex elements. The induced velocities at the blade elements and the strengths of bound vorticity are then computed and provided as outputs. This wake implementation was validated against both experimental and computational fluid dynamics (CFD) data at hover, forward flight, and vortex ring state in Ref. (23).

To account for ground effect, the method of images introduces a mirrored version of the rotor and its wake beneath the ground plane. In the inertial reference frame, this mirrored wake aligns with the original in the horizontal (x and y) directions but is positioned symmetrically in the vertical (z) axis, equal in magnitude and opposite in sign. The mirrored vortices carry the same strength as the actual ones. This arrangement ensures that the vertical component of the induced velocity at the ground cancels out, as the effects from the real and mirrored wakes are equal in magnitude but opposite in direction. When computing induced velocities at blade segments and collocation points, both the real wake and its image are included to capture the complete flow interaction near the ground (Ref. 26). An example implementation of the state-space free-vortex wake in ground effect is shown for a UH-60 in Fig. 5.

RESULTS AND DISCUSSION

In the present study, the collective pitch angle is fixed at 18° for all cases. The thrust coefficient, as well as its gradient computed per blade segment across the span and azimuth, is obtained using the free wake model to analyze an isolated rotor in full and inclined ground effect. The UH–60 rotor parameters used in the analysis are listed in Table 1.

To correlate the inflow predictions of the free wake model and the VPBFSM, the thrust coefficient gradient computed per blade segment from the free wake model is used as input to the VPBFSM. The pressure expansion coefficients in the VPBFSM are determined using Eq. (33), with the thrust coefficient gradient defined as:

$$\frac{dC_T}{d\bar{r}} = \frac{1}{\pi}\sum_{q=1}^{Q}\frac{L_q}{\rho\Omega^2 R^3} \tag{17}$$

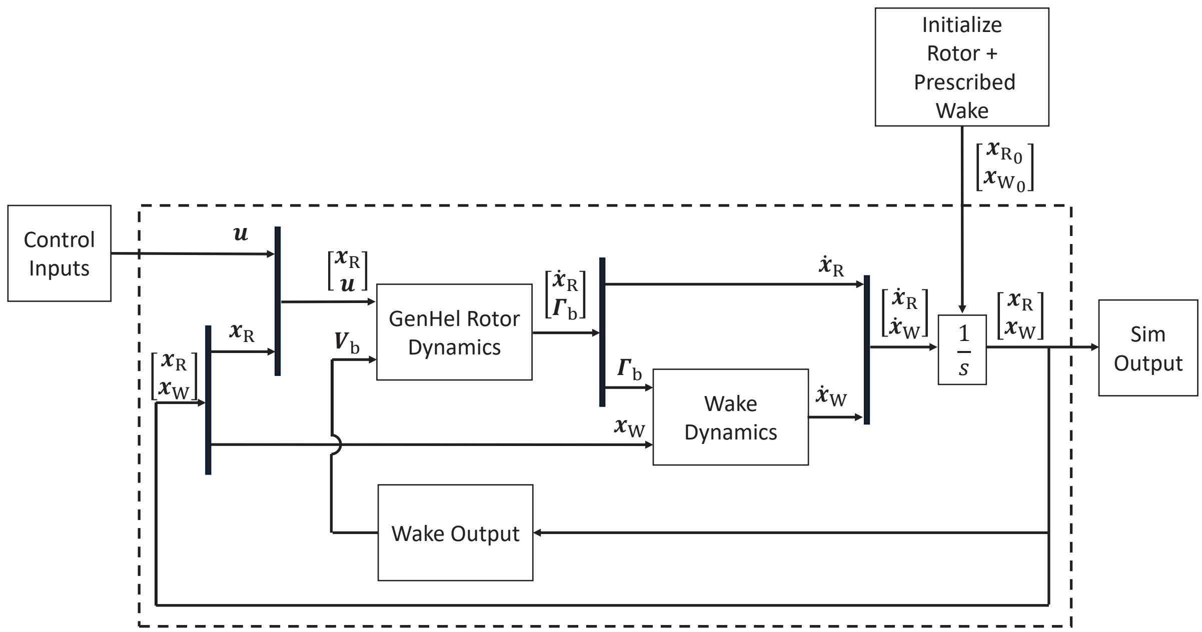

Figure 4: Schematic of coupled nonlinear state-space rotor-wake dynamics model.

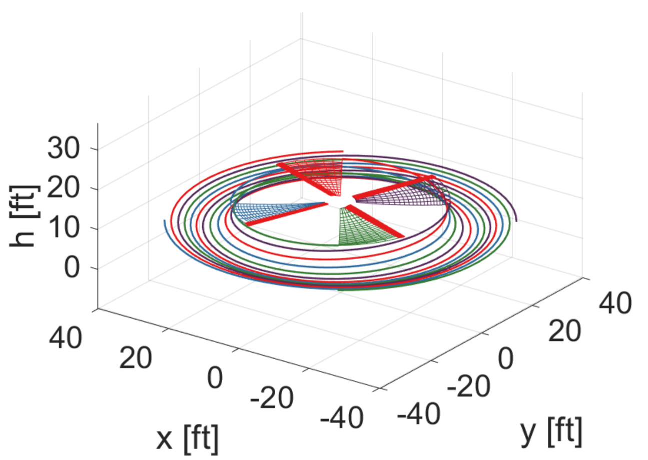

Figure 5: State-space free-vortex wake for a UH-60 helicopter experiencing ground effect at hover.

Table 1: UH–60 Rotor Parameters.

Parameter	Value	Units
Number of blades	4	-
Rotor radius	26.83	ft
Blade chord	20.76 / 20.965	in
Blade thickness	9.5	%
Rotor disk area	2261.5	ft^2
Rotor blade area	186.9	ft^2
Solidity ratio	0.0826	-
Blade tip sweep (aft)	20	deg
Airfoils	SC1095/SC1094 R8	-
Nominal rotor speed	258	RPM
Nominal tip speed	725	ft/sec

Full Ground Effect Case

Figure 6 shows the nondimensional thrust coefficient gradient obtained using the free wake model at different rotor heights above ground. For a fixed collective pitch angle, the thrust coefficient gradient increases as the rotor approaches the ground. This is due to the reduction in induced velocity near the ground plane, which leads to higher aerodynamic loading across the span, particularly near the mid-span and tip regions.

Figure 7 shows the nondimensional thrust coefficient gradient predicted by both models for the out-of-ground-effect (OGE) case. The VPBFSM uses three pressure expansion terms $(\tau_1^0, \tau_3^0, \tau_5^0)$ to represent the thrust coefficient gradient. As shown, the overall thrust gradient distribution of the VPBFSM matches that of the free wake model, with some deviations near the root and tip regions.

Near the root, the free wake model accounts for the blade root cutout, whereas the VPBFSM represents the distribution across the entire rotor span without explicitly modeling the cutout. Toward the tip, the free wake solution exhibits a sharp increase in the thrust gradient, influenced by tip vortices. To avoid numerical artifacts in this region, the free wake result near the tip is truncated. In contrast, the VPBFSM produces a smoother variation near both the tip and root due to its use of Legendre polynomial functions.

Three pressure expansion coefficient terms are used to represent the loading, as this is the minimum number required to

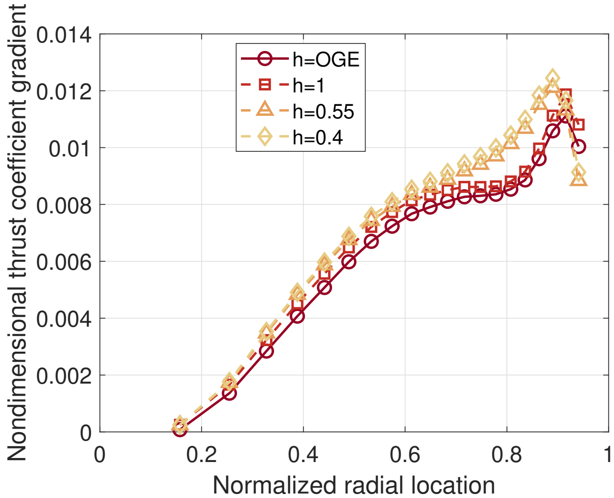

Figure 6: Nondimensional thrust coefficient gradient using free Wake model for different rotor heights.

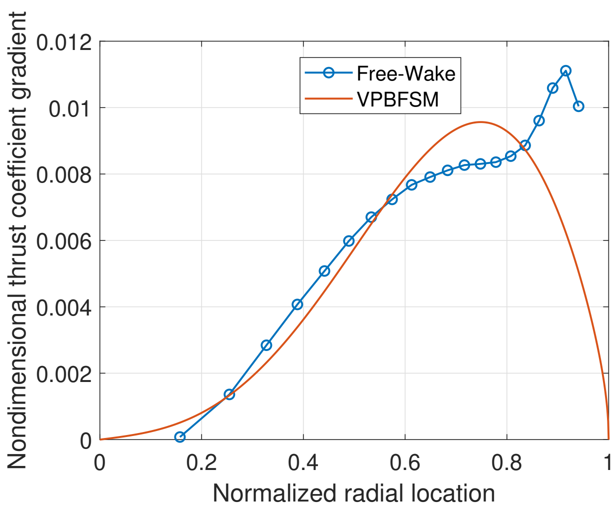

Figure 7: Nondimensional thrust coefficient gradient for the OGE case using both models.

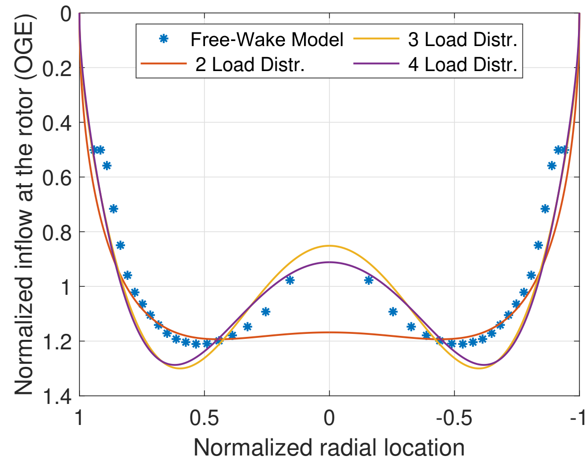

(a) Normalized inflow distribution using varying VPBFSM pressure expansion terms and the free wake model.

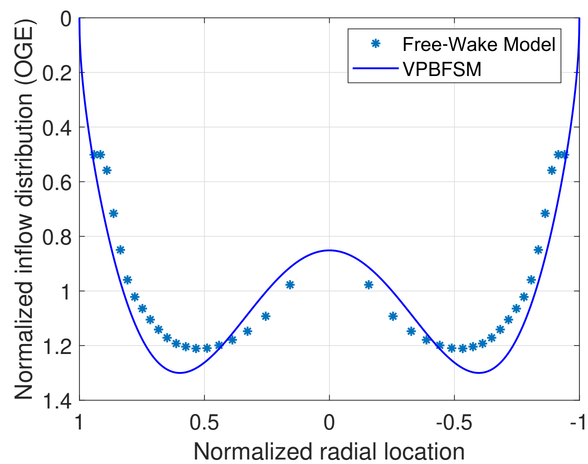

(b) Normalized rotor inflow distribution along the radius using three VPBFSM terms and the free wake model.

Figure 8: Normalized inflow distributions at the rotor for the OGE case using the VPBFSM with varying pressure expansion terms and the free wake model.

match the inflow distribution from the VPBFSM to the free wake model in the OGE case, as shown in Fig. 8a. The comparison in Fig. 8b further confirms the suitability of this expansion for capturing the radial inflow behavior. This number of terms is retained for the remainder of the analysis, including the full and inclined ground effect cases.

Note that all inflow distribution plots are normalized by the average inflow in the OGE case. In studying ground effect, Fig. 9 shows the normalized inflow distribution predicted by both models at a rotor height of $h = 1.0$. The VPBFSM result exhibits good agreement with the free wake model, indicating that the inflow behavior at this ground clearance is well captured by the VPBFSM. At each rotor height, the corresponding nondimensional thrust coefficient gradient from the free wake model is used as input to the VPBFSM to compute the inflow distribution in ground effect.

Moreover, Fig. 10 shows that the variation in inflow distribution with rotor height predicted by both models aligns with physical expectations. As the rotor approaches the ground, the inflow decreases due to the reduced clearance, which limits the downward induced flow. Figure 10a illustrates the inflow distribution from the free wake model, where a gap appears in the mid-span region corresponding to the blade root cutout. Near the tip, sharp variations are observed across different rotor heights, influenced by the presence of tip vortices. In contrast, the VPBFSM results in Fig. 10b exhibit a smoother inflow distribution that varies more uniformly with height, reflecting its representation of potential flow using Legendre polynomials. These results indicate that the VPBFSM reliably captures the inflow behavior across all rotor heights considered in this full ground effect case.

Inclined Ground Effect Case

For the inclined ground effect case, the non-dimensional thrust coefficient gradient as a function of radial position and

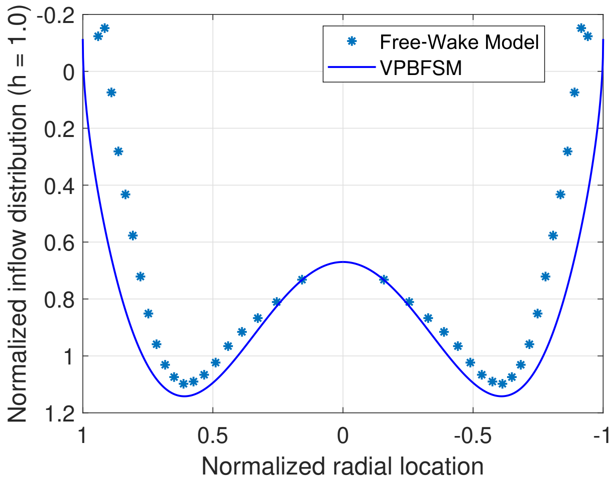

Figure 9: Normalized inflow distributions at the rotor for the case $h = 1.0$ using both models.

azimuthal angle, is first computed using the free wake model and then used to obtain the inflow distribution for both models. Figure 11 presents contours of the non-dimensional thrust coefficient gradient at $h = 1.0$ and $\delta = 15°$. Two regions of elevated loading appear: a primary peak at the outboard retreating side (azimuthal $\psi \approx 270°$ at the top of the contour plot) and a secondary peak near the inboard valley side (hub region). The advancing side exhibits the lowest gradients across most of the span, reflecting the combined effects of blade tilt and root cutout.

Figure 12 compares the resulting inflow distributions; the VPBFSM closely matches the free wake model on the valley side but exhibits some discrepancy on the mountain side. This discrepancy likely arises from tip vortex effects, which are captured by the free wake model but omitted in the VPBFSM. The free wake model tracks the evolving helical vortex geometry—allowing contraction and expansion near the blade tip—whereas the VPBFSM employs a rigid cylindrical wake formulation, resulting in a smoother inflow prediction on the mountain side.

Figure 13 presents contours of the non-dimensional thrust coefficient gradient at $h = 1.0$ for ground inclinations of 5°, 8°, 10°, 30°, and 40° (the 15° case is shown in Fig. 11). For the small tilts (5°, 8°, 10°), the largest gradients occur on the mountain side and the smallest on the valley side, reflecting the classic asymmetric loading of a slightly inclined disk.

Under more severe inclinations (30°, 40°), three spanwise regions emerge:

- Inboard region: A strong high-loading lobe appears on the valley side mid-span (left of center), even exceeding the mountain-side tip peak at 40°.
- Outboard region: The advancing side exhibits higher gradients than the retreating side.
- Tip region: The retreating-side tip shows higher gradients than the advancing-side tip.

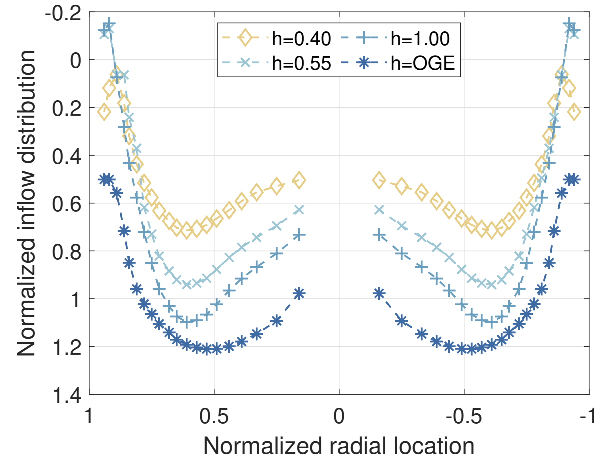

(a) Normalized inflow distribution at various rotor heights for the free wake model.

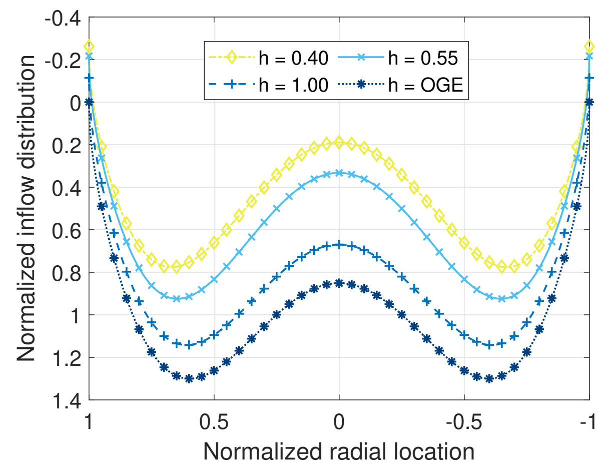

(b) Normalized inflow distribution at various rotor heights for the VPBFSM.

Figure 10: Normalized inflow distribution at various rotor heights for both models.

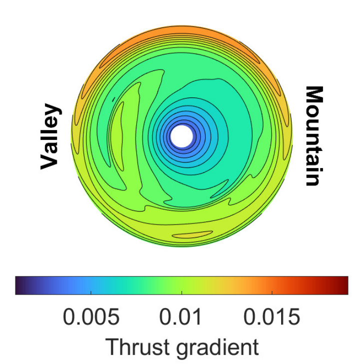

Figure 11: Nondimensional thrust coefficient gradient for the OGE case using free wake model at $h = 1$, and $\delta = 15°$.

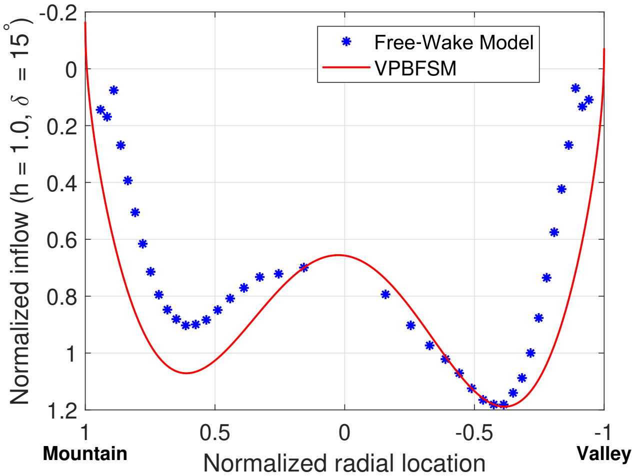

Figure 12: Normalized inflow distributions at the rotor for the case $h = 1.0$, and $\delta = 15^\circ$ using both models.

This redistribution of loading with increasing tilt highlights the growing influence of blade-element proximity to the ground.

Figure 14 compares the normalized inflow distributions at $h = 1.0$ for different ground inclinations 5°, 8°, 10°, 15°, 30°, and 40° as predicted by both models. In both models, increasing inclination reduces inflow on the mountain side and increases it on the valley side, reflecting the asymmetric ground-effect influence. While the overall trends agree closely, the two models show slight differences in absolute magnitude; this discrepancy is primarily due to tip-vortex effects, which are captured by the free wake model but not by the VPBFSM.

Figure 15 presents contours of the non-dimensional thrust coefficient gradient at $h = 0.9$ and $h = 1.5$ for a ground inclination of 30°. Figure 16 then compares the inflow distributions predicted by the two models. The VPBFSM closely matches the free wake model on the valley side, with some discrepancy on the mountain side. As discussed earlier, this discrepancy arises from tip-vortex effects captured by the free wake model but not by the VPBFSM.

CONCLUSIONS

This paper presents an evaluation of a reduced-order velocity potential-based finite state model (VPBFSM) against a high-fidelity free wake model for predicting rotor inflow in different types of ground effect, including full and inclined ground effect cases. The VPBFSM represents the lifting rotor as a pressure discontinuity in the flow field, while the ground is modeled using mass source distributions with strengths determined in terms of rotor loading to enforce the non-penetration of flow boundary condition. The free wake model incorporates the image rotor method to study an isolated rotor in ground effect, which automatically enforces the non-penetration of flow boundary condition at the ground.

The objective of this study is to evaluate the ability of the VPBFSM to predict the rotor inflow distribution in ground effect by comparing its predictions against the free wake model.

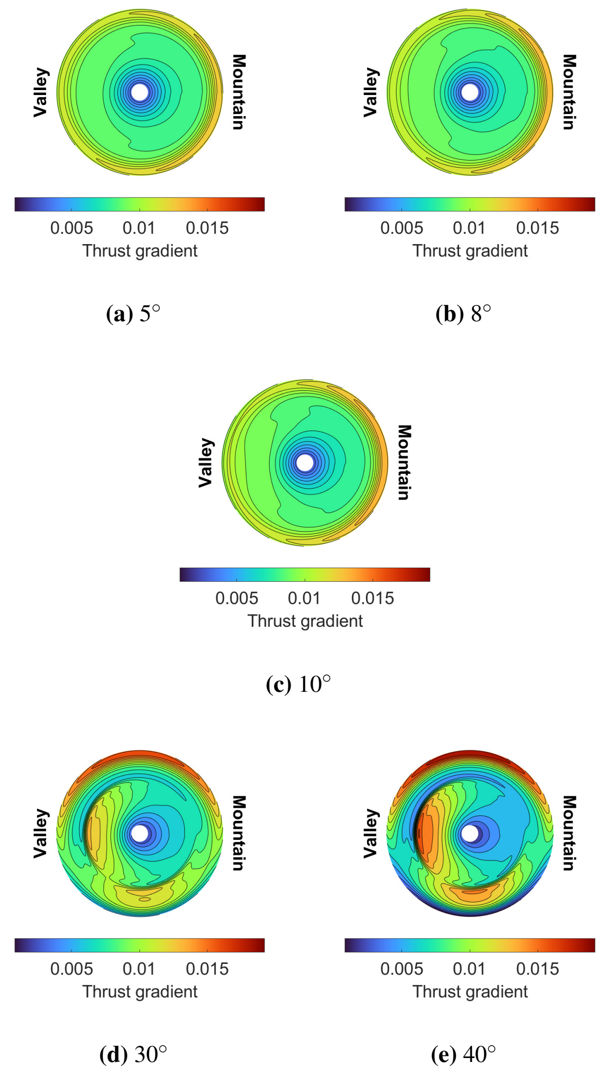

Figure 13: Contours of non-dimensional thrust coefficient gradient at $h = 1.0$ for inclinations of 5°, 8°, 10°, 30°, and 40°.

This evaluation builds confidence in applying the VPBFSM to analyze an isolated rotor in ground effect.

Key findings include:

- The VPBFSM accurately captures the inflow trends observed in the free wake model across all rotor heights in full ground effect, including the reduction in inflow as the rotor approaches the ground.
- At a fixed rotor height and various ground inclinations (up to 40°), the VPBFSM closely matches the free wake model's inflow predictions on the valley side, with some discrepancy on the mountain side. This discrepancy arises from tip-vortex effects: the free wake model allows vorticity roll-up and wake deformation, whereas the VPBFSM employs a rigid cylindrical wake distribution.
- At a fixed ground inclination and varying rotor heights, the VPBFSM closely matches the free wake model's in-

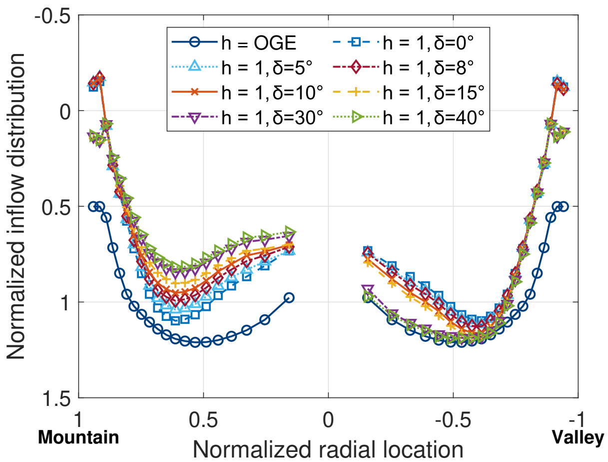

(a) Free wake model.

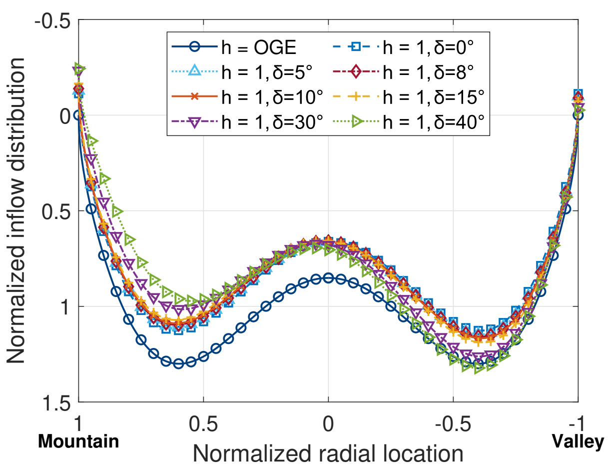

(b) VPBFSM.

Figure 14: Normalized inflow distribution at $h = 1.0$ and different inclination angles for both models.

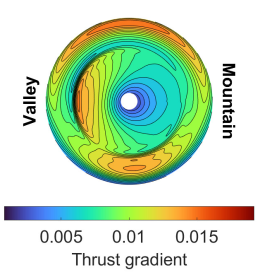

(a) $h = 0.9$

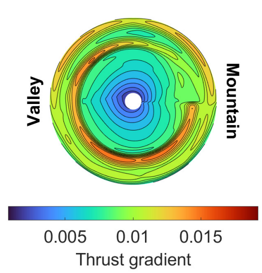

(b) $h = 1.5$

Figure 15: Contours of the non-dimensional thrust coefficient gradient at $h = 0.9$ and $h = 1.5$ for a ground inclination of $30°$.

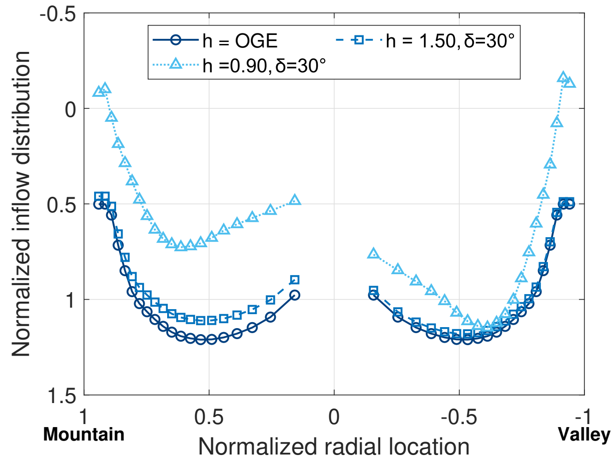

(a) Free wake model.

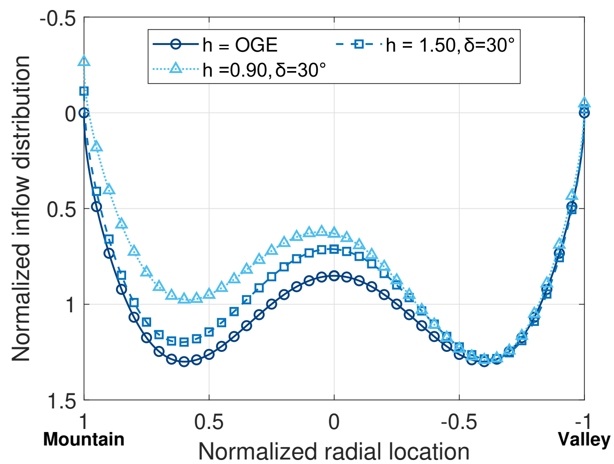

(b) VPBFSM.

Figure 16: Normalized inflow distributions for the VPBFSM and free wake model at a ground inclination of $30°$ and various rotor heights.

flow distributions, with only slight mountain side differences due to tip-vortex effects.

Finally, the proposed VPBFSM approach represents rotor inflow distribution in both normal and inclined ground effect cases, consistent with physical expectations and in close agreement with the free wake model. Future studies should evaluate the VPBFSM approach against experimental data to build further confidence in its predictions and extend the analysis to dynamic ground effect cases.

Authors contact:
Andro Metry ametry3@gatech.edu
J.V.R. Prasad jvr.prasad@ae.gatech.edu
Cecilia Cannone ccannone@umd.edu
Batin Bugday bugday@umd.edu
Umberto Saetti saetti@umd.edu

APPENDIX A

ELLIPSOIDAL COORDINATE SYSTEM

The ellipsoidal coordinate system $(\nu, \eta, \bar{\psi})$ is defined as:

$$\bar{x} = -\sqrt{1-\nu^2}\sqrt{1+\eta^2}\cos(\bar{\psi}) \tag{18a}$$

$$\bar{y} = \sqrt{1-\nu^2}\sqrt{1+\eta^2}\sin(\bar{\psi}) \tag{18b}$$

$$\bar{z} = -\nu\eta \tag{18c}$$

where $\bar{x}, \bar{y}, \bar{z}$ are the Cartesian coordinates normalized with rotor radius. The values of $\nu, \eta, \bar{\psi}$ cover entire 3-dimensional space if they are restricted to the following ranges:

$$-1 \le \nu \le 1 \tag{19a}$$

$$0 \le \eta \le \infty \tag{19b}$$

$$0 \le \bar{\psi} \le 2\pi \tag{19c}$$

Figure 17 shows the ellipsoidal coordinate system viewed in the $\bar{x}-\bar{z}$ plane. While ν defines constant hyperboloid surfaces, η defines constant ellipsoid surfaces. Both families of surfaces are azimuthally symmetric about the $\bar{z}-axis$. When $\eta = 0$, surfaces represent the two faces of the disk, and ν changes sign across the disk. The inverse of Eqs. $(18a)$ through $(18c)$ is given as:

$$\nu = -\frac{\text{sign}(\bar{z})}{\sqrt{2}}\sqrt{(1-\bar{S})+\sqrt{(1-\bar{S})^2+4\bar{z}^2}} \tag{20a}$$

$$\eta = \frac{1}{\sqrt{2}}\sqrt{(\bar{S}-1)+\sqrt{(\bar{S}-1)^2+4\bar{z}^2}} \tag{20b}$$

$$\bar{\psi} = \tan^{-1}\left(\frac{-\bar{y}}{\bar{x}}\right) \tag{20c}$$

where:

$$\bar{S} = \bar{x}^2+\bar{y}^2+\bar{z}^2 \tag{21}$$

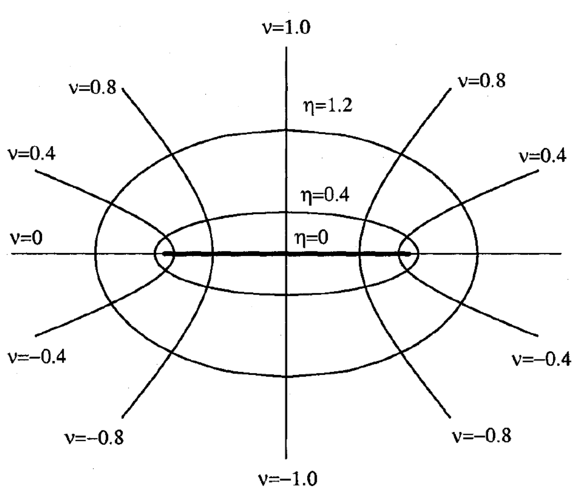

Figure 17: Ellipsoidal coordinate system.

APPENDIX B

NORMALIZED ASSOCIATED LEGENDRE FUNCTIONS

This appendix presents the normalized associated Legendre functions (Refs. 28, 29). $\bar{P}_n^m(\nu)$ and $\bar{Q}_n^m(i\eta)$ are normalized associated Legendre functions of the first and second kind, respectively (Refs. 37, 38).

$$\bar{P}_n^m = (-1)^m \frac{P_n^m(\nu)}{\rho_n^m} \tag{22a}$$

$$\bar{Q}_n^m = \frac{Q_n^m(i\eta)}{Q_n^m(i0)} \tag{22b}$$

where:

$$(\rho_n^m)^2 = \int_0^1 [P_n^m(\nu)]^2 d\nu = \frac{1}{2n+1}\frac{(n+m)!}{(n-m)!} \tag{23a}$$

$$Q_n^m(i0) = \begin{cases} \frac{\pi}{2}(-1)^{n+m+1}(i)^{n+1}\frac{(n+m-1)!!}{(n-m)!!} & n+m = \text{even} \\ (-1)^{n+m+1}(i)^{n+1}\frac{(n+m-1)!!}{(n-m)!!} & n+m = \text{odd} \end{cases} \tag{23b}$$

Further details on the associated Legendre functions $P_n^m(\nu)$ and $Q_n^m(i\eta)$, as well as their normalized forms, can be found in Refs. (28, 29).

APPENDIX C

APPENDIX C:AXIAL INDUCED VELOCITY COMPONENT

This appendix reviews the derivation of an equation to compute the velocity on and above the rotor disk. A detailed derivation is provided in Ref. (6). In general, velocity can be expressed as the gradient of the velocity potential:

$$\vec{v} = \vec{\nabla}\Psi \tag{24}$$

where $\vec{v}$ is the velocity vector and Ψ is the velocity potential.

The velocity potential consists of time-dependent and spatially dependent components, namely the velocity potential states (a_n^m) for time dependency and the velocity potential function $(\tilde{\Psi}_n^m)$ for spatial dependency. Thus, Eq. (24) can be rewritten for the cosine term as:

$$\vec{v} = \sum_{m=0}^{\infty}\sum_{n=m+1}^{\infty}(a_n^m \vec{\nabla}\tilde{\Psi}_n^{mc}) \tag{25}$$

where:

$$\tilde{\Psi}_n^{mc} = \sigma_n^m \Phi_{n+1}^{mc} + \zeta_n^m \Phi_{n-1}^{mc} \tag{26}$$

Here, σ and ζ are constants defined in Ref. **?**, and Φ is the pressure potential (shaping function).

Taking the gradient of Eq. (26) in the axial direction gives:

$$\frac{\partial \tilde{\Psi}_n^{mc}}{\partial z} = \frac{\partial(\sigma_n^m \Phi_{n+1}^{mc} + \zeta_n^m \Phi_{n-1}^{mc})}{\partial z} = \Phi_n^{mc}, \quad n > m \tag{27}$$

The final expression for the velocity on and above the rotor disk is:

$$\vec{v}_z = \sum_{m=0}^{\infty} \sum_{n=m+1}^{\infty} a_n^m \frac{\partial \tilde{\Psi}_n^{mc}}{\partial z} = \sum_{m=0}^{\infty} \sum_{n=m+1}^{\infty} a_n^m \Phi_n^{mc} \tag{28}$$

where:

$$\Phi_n^{mc} = \bar{P}_n^m(\nu)\bar{Q}_n^m(i\eta)\cos(m\bar{\psi}) \tag{29}$$

APPENDIX D

CORRELATION MATRICES FOR GROUND EFFECT

This appendix discusses the correlation matrices for ground effect. Each rotor produces two types of velocity: the first is the self-flow (induced) velocity of the rotor, and the second is the velocity induced by the interaction between the main rotor and the ground rotor.

The self-flow velocity of the main rotor and ground can be computed using the following equation:

$$\vec{v}_{\text{SelfRotor}} = \sum_{m=0}^{\infty} \sum_{n}^{\infty} a_n^m \Phi_n^{mc} \tag{30}$$

The key distinction between the self-flow velocity of the ground and main rotors lies in the radial distribution (n). For the self-flow velocity of the main rotor, $n = m+1, m+3...$, whereas the self-flow velocity of the ground rotor, $n = m+2, m+4....$ To differentiate between the velocity states, harmonics, and radial terms of the main rotor and ground rotor, we define a as c for the ground rotor, where m becomes r, and n becomes j. This means that a_n^m will be c_j^r for ground rotor. It is also important to note that $r = j$ terms are excluded in computing the ground flow velocities to avoid singularities, as discussed in Refs. (6, 10).

Furthermore, Fig. 1 illustrates the coordinate system used to compute induced velocities below the rotor within the wake radius (Ref. 29). The velocity at a given point below the rotor is computed as:

$$\vec{v}_A = \vec{v}_B + \vec{v}_C^{\dagger} - \vec{v}_D^{\dagger} \tag{31}$$

where ($\vec{v}_A$) is the wake velocity at the ground ($\vec{v}_{MainOnGround}$), ($\vec{v}_B$) is the induced velocity on the rotor disk, ($\vec{v}_C^{\dagger}$) is the adjoint induced velocity on the rotor disk, and ($\vec{v}_D^{\dagger}$) is the adjoint induced velocity above the rotor disk.

For the steady-state assumption, the adjoint states $\vec{v}_c^{\dagger}$ and $\vec{v}_D^{\dagger}$ are independent of time, leading to the simplified expression:

$$\vec{v}_A = 2\vec{v}_B - \vec{v}_D \tag{32}$$

Additionally, for steady-state, the strengths of the mass source distributions at the ground rotor are estimated by equating the main rotor's wake velocity at the ground to the exit flow velocity of the mass source distributions at the ground:

$$\vec{v}_{\text{Main On Ground}} = \vec{v}_{\text{SelfGround}} \tag{33}$$

where:

$$\vec{v}_{\text{MainOnGround}} = \sum_{m=0}^{\infty} \sum_{n=m+1}^{\infty} a_n^m (2\Phi_n^{mc}|_{\text{Self Rotor}} - \Phi_n^{mc}|_{\text{Above Rotor}}) \tag{34}$$

$$\vec{v}_{\text{SelfGround}} = \sum_{r=0}^{\infty} \sum_{j=r+2}^{\infty} c_j^r \Phi_j^{rc}|_{\text{Self Ground}} \tag{35}$$

After substituting Eq. (34) and Eq. (35) in Eq. (33) and applying the orthogonality properties of the normalized associated Legendre function, a general relation between velocity states of the ground and the main rotor can be derived:

$$c_j^r = [G_{jn}^{rm}] a_n^m \tag{36}$$

$$r = 0,1 \quad j = r+2, r+4 \quad m = 0,1 \quad n = m+1, m+3$$

where $[G_{jn}^{rm}]$ is the velocity correlation matrix, expressed as:

$$G_{jn}^{rm} = 2\int_0^1 \bar{P}_j^r(\nu_2)\bar{P}_n^m(\nu_1)d\nu_2 - \int_0^1 \bar{P}_j^r(\nu_2)\bar{P}_n^m(\nu_1)\bar{Q}_n^m(i\eta_1)d\nu_2 \tag{37}$$

Here, $\bar{P}$ and $\bar{Q}$ are the normalized associated Legendre functions of the first and second kinds, respectively, and the subscripts 1 and 2 correspond to the main rotor and ground rotor, respectively. It is recommended to use the trapezoidal rule to solve the integration of this equation as the variable ν may not be equidistant.

For steady state conditions, the strengths of the mass source distributions at the ground can be related to the load distribution at the main rotor using the relation between velocity potential states and pressure terms:

$$\begin{Bmatrix} \tau_n^m = [V_L]_{\text{rotor}}\ a_n^m \\ \omega_j^r = [V_L]_{\text{ground}}\ c_j^r \end{Bmatrix} \tag{38}$$

where τ and ω are pressure coefficients corresponding to load distribution (main rotor) and mass source distribution (ground rotor), respectively. $[V_L]_{rotor}$, $[V_L]_{ground}$ are the mass flow parameters for the main rotor and the ground rotor, respectively. The mass flow parameter for the ground is defined as a diagonal matrix with twice the average of the main rotor velocity out of ground at the diagonal. The mass flow parameter for the main rotor is defined the same as the ground rotor, except the first element in the matrix is only the average out-of-ground velocity of the main rotor, which corresponds to a_1^0.

A direct relationship between the strengths of the mass source distributions at the ground rotor and the load distributions at the main rotor is obtained by substituting Eq. (38) in Eq. (36):

$$\omega_j^r = [S_{jn}^{rm}]\tau_n^m$$

$$r = 0,1 \quad j = r+2, r+4 \quad m = 0,1 \quad n = m+1, m+3 \tag{39}$$

where $[S_{jn}^m]$ is the pressure correlation matrix:

$$[S_{jn}^{rm}] = [V_e][G_{jn}^{rm}]$$

$$r = 0,1 \quad j = r+2, r+4 \quad m = 0,1 \quad n = m+1, m+3 \tag{40}$$

with V_e defined as:

$$V_e = \begin{bmatrix} 2 & & & 0 \\ & 1 & & \\ & & \ddots & \\ 0 & & & 1 \end{bmatrix} \tag{41}$$

Since in this paper, even pressure coefficients and velocity potential states are used for the ground rotor finite state equation so the first element in the mass flow matrix is twice the average velocity of the main rotor out-of-ground effect. However, if odd velocity potential states are used including c_1^0 then V_e will be an identity matrix.

The general form of expressing the strengths of the mass source distributions in terms of rotor loading is:

$$\begin{aligned}
\omega_j^{0c} &= \frac{1}{2\pi}\sum_{m=0}^{\infty}\sum_{n=m+1}^{\infty}\int_0^{2\pi} S_{jn}^{rm}(\tau_n^{mc}\cos m\bar{\psi}_1 + \tau_n^{ms}\sin m\bar{\psi}_1)\cos r\bar{\psi}_2\, d\bar{\psi}_2 \\
\omega_j^{rc} &= \frac{1}{\pi}\sum_{m=0}^{\infty}\sum_{n=m+1}^{\infty}\int_0^{2\pi} S_{jn}^{rm}(\tau_n^{mc}\cos m\bar{\psi}_1 + \tau_n^{ms}\sin m\bar{\psi}_1)\cos r\bar{\psi}_2\, d\bar{\psi}_2 \\
\omega_j^{rs} &= \frac{1}{\pi}\sum_{m=0}^{\infty}\sum_{n=m+1}^{\infty}\int_0^{2\pi} S_{jn}^{rm}(\tau_n^{mc}\cos m\bar{\psi}_1 + \tau_n^{ms}\sin m\bar{\psi}_1)\sin r\bar{\psi}_2\, d\bar{\psi}_2
\end{aligned} \tag{42}$$

APPENDIX E

INCLUSION OF THE MISSING TERMS IN THE CORRELATION MATRICES FOR GROUND EFFECT

This appendix explains how to include the missing terms in both the correlation matrices and the ground flow velocity calculations for analyzing rotor ground effect. The correlation matrices developed in Appendix D exclude the $r = j$ terms to avoid singularities, as discussed in Refs. (6, 10). It is also noted in Eq. (27) that the formulations are only valid for $r \neq j$ ($m \neq n$). Ref. (30) proposes the following velocity potential formulation to avoid singularities:

$$\tilde{\Psi}_r^{rc} = [\sigma_r^r \bar{P}_{r+1}^r(\nu)\bar{Q}_{r+1}^r(i\eta) + \bar{P}_{r-1}^r(\nu)\bar{Q}_{r-1}^r(i\eta)]\cos(r\bar{\psi}) \tag{43a}$$

$$\tilde{\Psi}_r^{rs} = [\sigma_r^r \bar{P}_{r+1}^r(\nu)\bar{Q}_{r+1}^r(i\eta) + \bar{P}_{r-1}^r(\nu)\bar{Q}_{r-1}^r(i\eta)]\sin(r\bar{\psi}) \tag{43b}$$

where:

$$\bar{P}_{r-1}^r = \frac{2}{\pi}\sqrt{\frac{(2r)!!}{(2r+1)!!}}\frac{(1-\nu^2)^{r/2}}{(1+\nu)^r}\sum_{j=0}^{r-1}\frac{(r-1)!2^{r-j-1}(-1)^j}{(r-j-1)!(r+j)} \tag{44a}$$

$$(1-\nu)^j \tag{44b}$$

$$\bar{Q}_{r-1}^r = \frac{1}{(1+\eta^2)^{r/2}} \tag{44c}$$

Even with Eq. (44b), a singularity persists for the case $r = j = 0$. This singularity can be avoided using the following expression:

$$\begin{aligned}
\tilde{\Psi}_0^0 = &\frac{2}{\pi}\nu\left[1 - \eta\tan^{-1}\left(\frac{1}{\eta}\right)\right] - \frac{2}{\pi}\ln|1+\nu| - \frac{1}{\pi}\ln|a+\eta^2| \\
&+ \frac{2}{\pi}\ln(R_{\max})
\end{aligned} \tag{45}$$

where R_{max} is a large number that represents the radius of integration along the free-stream direction, ξ.

The velocity and pressure correlation matrices will be computed using the same procedure since the approximate solution in Ref. (30) relates the gradient of the velocity potential to the pressure potential. Thus, the strengths of the mass source distributions at the ground needed to impose the boundary condition can be determined using Eq. (42).

While including the missing terms ensures the boundary condition is imposed, it also amplifies the ground effect on the main rotor. To mitigate this effect, an empirical correction factor is applied to the gradient of the velocity potential, reducing the influence of the sources on the main rotor. This factor is devised to preserve the gradient of the velocity potential at the ground—since the boundary condition is satisfied—while rapidly diminishing the influence of sources as the distance from the source distribution increases. This empirical correction factor, given by Eq. (47), was originally calibrated at a rotor height of $h = 1$, using the ground effect factor from Hayden's model in the case study presented in Ref. (15), and is applied unchanged in the current study.

The corrected form of the gradient of the velocity potential of the $r = j$ terms is given by:

$$\frac{\partial\tilde{\Psi}_r^{rc}}{\partial z} = \left(\frac{\pi}{7}\right)^{\eta^2}\bar{P}_r^r(\nu)\bar{Q}_r^r(i\eta)\cos(r\bar{\psi}) \tag{46}$$

where:

$$\left(\frac{\pi}{7}\right)^{\eta^2} = \begin{cases} 1, & \eta = 0 \quad \text{(at ground)} \\ 0, & \eta \to \infty \quad \text{away from ground} \end{cases} \tag{47}$$

ACKNOWLEDGMENTS

This research was partially funded by the U.S. Government under Cooperative Agreement No. W911W6-21-2-0001. The U.S. Government is authorized to reproduce and distribute reprints for Government purposes notwithstanding any copyright notation thereon.

The views and conclusions contained in this document are those of the authors and should not be interpreted as representing the official policies of position, either expressed or implied, of the U.S. Army Combat Capabilities Development Command (DEVCOM), Aviation & Missile Center (AvMC), or the U.S. Government.

REFERENCES

1. Zhang, H., Prasad, J. V. R., and Peters, D. A., "Finite State Inflow Models for Lifting Rotors in Ground Effect," American Helicopter Society 52nd Annual Forum Proceedings, Vol. 2, June 1996.

2. Prasad, J. V. R., Zhang, H., and Peters, D. A., "Finite State in-Ground Effect Inflow Models for Lifting Rotors," American Helicopter Society 53rd Annual Forum Proceedings, Vol. 2, April 1997.

3. Xin, H., Prasad, J. V. R., and Peters, D. A., "Dynamic Inflow Modeling for Simulation of a Helicopter Operating in Ground Effect," Proceedings of AIAA Modeling and Simulation Technology Conference, Paper No. AIAA-99-4114, August 1999.

4. Xin, H., Prasad, J. V. R., and Peters, D. A., "Inflow Modeling for Simulation of Helicopter Flight in Dynamic Ground Effect," Proceedings of the 25th European Rotorcraft Forum, September 1999.

5. Xin, H., *Development and Validation of a Generalized Ground Effect Model for Lifting Rotors*, Georgia Institute of Technology, 1999.

6. Morillo, J. A., and Peters, D. A., "Velocity Field Above a Rotor Disk by a New Dynamic Inflow Model," *Journal of Aircraft*, Vol. 39, (5), 2002, pp. 731–738.

7. Peters, D. A., Morillo, J. A., and Nelson, A. M., "New Developments in Dynamic Wake Modeling for Dynamics Applications," *Journal of the American Helicopter Society*, Vol. 48, (2), April 2003, pp. 120–127.

8. Yu, K., and Peters, D. A., "Use of Potential Flow State-Space Inflow Modeling for Mass Source Rotors," Proceedings of the 29th European Rotorcraft Forum, September 2003.

9. Yu, K., and Peters, D. A., "Net Mass Flow Components in a Three-Dimensional Unsteady Rotor Inflow Model," Proceedings of ASME International Mechanical Engineering Congress and Exposition 2003, Paper No. IMECE2003-42459, November 2003.

10. Yu, K., and Peters, D. A., "Nonlinear State-Space Modeling of Dynamic Ground Effect," *Journal of the American Helicopter Society*, Vol. 50, (3), 2005, pp. 259–268.

11. Metry, A., Prasad, J. V. R., and Peters, D. A., "Finite State Modeling of Ground Effect Using Mass Source Distribution at the Ground Plane," Proceedings of the 80th Vertical Flight Society Forum, May 2024.

12. Guner, F., Prasad, J. V. R., and Peters, D. A., "An Approximate Finite State Dynamic Wake Model for Predictions of Inflow below the Rotor," *Journal of the American Helicopter Society*, Vol. 66, (3), July 2021, pp. 1–10. DOI: 10.4050/JAHS.66.032007

13. Guner, F., Prasad, J. V. R., He, C., and Peters, D. A., "Fidelity Enhancement of a Multi-Rotor Dynamic Inflow Model via System Identification," *Journal of the American Helicopter Society*, Vol. 67, (2), April 2022, pp. 1–17. DOI: 10.4050/JAHS.67.022009

14. Metry, A., Prasad, J. V. R., and Peters, D. A., "A Velocity Potential Based Finite State Modeling of Ground Effect," Proceedings of the 50th European Rotorcraft Forum, 2024.

15. Metry, A., Prasad, J. V. R., and Peters, D. A., "A Velocity Potential-Based Finite State Model for Ground Effect Analysis," Proceedings of the 81st Vertical Flight Society Forum, May 2025.

16. Hayden, J. S., "The Effect of the Ground on Helicopter Hovering Power Required," Proc. AHS 32nd Annual Forum, 1976.

17. Keller, J., McKillip, R., Wachspress, D., Tischler, M., and Juhasz, O., "Linearized Inflow and Interference Models from High Fidelity Free Wake Analysis for Modern Rotorcraft Configurations," Proceedings of the 75*th* Annual Forum of the Vertical Flight Society, May 14-15, 2019.

18. He, C., Syal, M., Tischler, M., and Juhasz, O., "State-Space Inflow Model Identification from Viscous Vortex Particle Method for Advanced Rotorcraft Configurations," Proceedings of the 73*rd* Annual Forum of the Vertical Flight Society, May 9-11, 2017.

19. Celi, R., "State-Space Representation of Vortex Wakes by the Method of Lines," *Journal of the American Helicopter Society*, Vol. 50, (2), Apr 2005, pp. 195–205. DOI: https://10.4050/1.3092855

20. Saetti, U., "Linearization of a Rotor Simulation with a State-Space Free-Vortex Wake Model in a Shipboard Environment," Proceedings of the AIAA Aviation Forum, Chicago, IL & Virtual, Jun 27 - Jul 1, 2022. DOI: https://doi.org/10.2514/6.2022-3646

21. Saetti, U., and Horn, J. F., "Implementation and Linearization of State-Space Free-Vortex Wake Models for Rotary- and Flapping-Wing Vehicles," *Journal of the American Helicopter Society,* Article in Advance, Apr 2023. DOI: https://doi.org/10.4050/JAHS.68.042004

22. Saetti, U., and Bugday, B., "Tiltrotor Simulations with Coupled Flight Dynamics, State-Space Aeromechanics, and Aeroacoustics," *Journal of the American Helicopter Society*, **68**, 012003 (2024). DOI: https://doi.org/10.4050/JAHS.69.012003

23. Bugday, B., Saetti, U., Manhji, A. K., and Horn, J. F., "Validation of a State-Space Free Wake Model with a Near-Wake Vortex Lattice Model," Proceedings of the 78$^{\text{th}}$ Annual Forum of the Vertical Flight Society, May 20-22, 2025. DOI: https://doi.org/10.4050/F-0081-2025-155

24. Saberi, H., and Maisel, M. D., "AFreeWake Rotor-Analysis Including Ground Effect," Proceedings of the 43rd Annual Forum of the American Helicopter Society, 1987.

25. Brown, R. E., and Whitehouse, G. R., "Modeling Rotor Wakes in Ground Effect," *Journal of the American Helicopter Society*, Vol. 49, (3), 2005, pp. 238–249. DOI: https://doi.org/10.4050/JAHS.49.238

26. Griffiths, D. A., Ananthan, S., and Leishman, J., "Predictions of Rotor Performance in Ground Effect Using a Free-VortexWake Model," *Journal of the American Helicopter Society*, **50**, 012003 (2005). DOI: https://doi.org/10.4050/jahs.62.012006

27. Saetti, U., "Real-Time Simulation of a Shipborne Rotor via Linearized State-Space Free-Vortex Wake Models," *Journal of Aircraft*, Vol. 61, (3), 2024, pp. 1025–1033. DOI: https://doi.org/10.2514/1.C037389

28. He, C., *Development and Application of a Generalized Dynamic Wake Theory for Lifting Rotors*, Ph.D. thesis, Georgia Institute of Technology, July 1989.

29. Fei, Z., *A Rigorous Solution for Finite-State Inflow Throughout the Flowfield*, Ph.D. thesis, Washington University in St. Louis, May 2013.

30. Mong-che, A. H., "A Complete, Finite-State Model for Rotors in Axial Flow," *Master of Science Thesis, Washington University in St. Louis*, 2006.

31. Horn, J. F., "Non-Linear Dynamic Inversion Control Design for Rotorcraft," *Aerospace*, Vol. 6, (38), 2019. DOI: https://doi.org/10.3390/aerospace6030038

32. Howlett, J. J., "UH-60A Black Hawk Engineering Simulation Program. Volume 1: Mathematical Model," Technical report, NASA-CR-166309, 1980.

33. Pitt, D. M., and Peters, D. A., "Theoretical Prediction of Dynamic-Inflow Derivatives," Proceedings of the 6$^{\text{th}}$ European Rotorcraft and Powered Lift Aircraft Forum, September 16-19, 1980.

34. Bagai, A., and Leishman, G. J., "Rotor Free-Wake Modeling Using a Pseudo-Implicit Technique—Including Comparison with Experimental Data," *Journal of the American Helicopter Society*, Vol. 40, (3), Jul 1995, pp. 29–41. DOI: https://doi.org/10.4050/JAHS.40.29

35. Bhagwat, M. J., *Transient Dynamics of Helicopter Rotor Wakes Using a Time-Accurate Free-Vortex Method*, Ph.D. thesis, University of Maryland, College Park, MD, 2001.

36. Saetti, U., and Horn, J. F., "Implementation and Linearization of a Rotor Simulation with a State-Space Free-Vortex Wake Model," Proceedings of the 78$^{\text{th}}$ Annual Forum of the Vertical Flight Society, May 10-12, 2022. DOI: https://doi.org/10.4050/F-0078-2022-17577

37. Gradshteyn, I. S., and Ryzhik, I. M., *Table of Integrals, Series, and Products*, Academic Press, New York, 1980, pp. 948–965.

38. Abramowitz, M., and Stegun, I. A., *Handbook of Mathematical Functions*, Academic Press, New York, 1970, pp. 332–341.